



Development of a dielectrically consistent reference interaction site model combined with the density functional theory for electrochemical interface simulations

Satoshi Hagiwara ^{1,*}, Satomichi Nishihara,² Fumiaki Kuroda ¹ and Minoru Otani^{1,†}

¹Center for Computational Sciences, University of Tsukuba, 1-1-1, Tenno-dai, Tsukuba, Ibaraki 305-8577, Japan

²AdvanceSoft Corporation, 4-3, Kanda Suruga-dai, Chiyoda-ku, Tokyo 101-0062, Japan



(Received 28 April 2022; accepted 6 September 2022; published 19 September 2022)

The dielectrically consistent reference interaction site model (DRISM) is one of the methods used to solve the well-known drawback of the reference interaction site model (RISM) theory: That it underestimates the dielectric constant of the solutions. Recently, Nishihara and Otani developed the first-principles effective screening medium (ESM) method combined with RISM theory, called ESM-RISM, to simulate physical properties at the electrode/electrolyte interface [Phys. Rev. B **96**, 115429 (2017)]. In this study, we combined DRISM with the ESM-RISM framework to increase the accuracy of electrochemical interface simulations, which was applied to the Pt(111)/aqueous water interface as a benchmark calculation. The electrochemical properties at the interface, such as the potential of zero charge, standard hydrogen electrode potential, and double-layer capacitance, all reasonably agree with previous experiments. The thickness of the contact layer was found to correlate well with double-layer capacitance. We believe that the present method is a useful tool to better model the physical properties at electrochemical interfaces.

DOI: [10.1103/PhysRevMaterials.6.093802](https://doi.org/10.1103/PhysRevMaterials.6.093802)

I. INTRODUCTION

An interface between electrode and electrolyte called the “electrochemical interface” is a fundamental reaction field that is important in electrochemical, catalytic, and corrosive reactions. At the electrochemical interface, both the outcome of the chemical reaction and its process depend on the electrode potential, types of electrolyte and solvent, concentrations of the electrolyte solutions, and solution temperature. Thus, controlling the combination of electrode and solution materials and the environmental parameters of the solution have the capability to improve the electrochemical properties of rechargeable batteries, fuel cells, catalysts, and anticorrosion technology. Therefore, the material properties at the electrochemical interface have attracted considerable attention from both experimental and theoretical researchers [1–4].

Theoretically, first-principles molecular dynamics (FPMD) is a powerful tool for simulating electrochemical reactions at electrochemical interfaces [5–12]. However, the FPMD method incurs large computational costs to obtain convergent thermodynamic properties owing to the necessary explicit treatment of electronic structures for all atoms comprising an interface. Furthermore, it is difficult for FPMD to apply a bias voltage to the half-cell system. The bias voltage provides excess charge to the electrode surface, and a counter ion originates from the bulk electrolyte solution to screen the surface charge. This mechanism corresponds to the formation of the electric double layer (EDL). However, FPMD cannot flexibly describe the counter ion for a half-cell system because of the

fixed number of atoms able to be modeled. Therefore, a more flexible method for describing the electrochemical interfaces is indispensable.

The hybrid simulation method consisting of first principles and implicit solution methods is a flexible method for computing the electrode/electrolyte system [13–19]. In the hybrid simulation method, the computational accuracy of the solution depends on the implicit solution theory [20]. There are many types of implicit solution theories used for simulating electrochemical problems, e.g., the conductor-like polarizable continuum model [14,21], the solvation model based on density [15,22,23], the charge-asymmetric nonlocally determined local-electric model [18,24,25], the conductor-like screening model for real solvents [16,26], a revised self-consistent continuum solvation model [17,27], and so on. The reference interaction site model (RISM) based on the Ornstein-Zernike-type integral equation is an accurate and flexible implicit solution theory [28–30]. Recently, Nishihara and Otani developed density functional theory (DFT) [31,32] using the effective screening medium (ESM) technique [33–37] combined with the Laue-represented RISM (LRISM) equation, called ESM-RISM, to simulate electrochemical reactions at the electrochemical interface [38]. ESM-RISM was developed as an extension of the three-dimensional RISM (3D-RISM) method [39,40] under a grand-canonical ensemble. Therefore, ESM-RISM naturally describes the formation of an EDL under a finite bias voltage [41,42].

Although the modeling of the ESM-RISM method is physically reasonable, a well-known drawback of the RISM theory is that it underestimates the dielectric constant of a solution with dipolar solvent molecules. Dielectrically consistent RISM (DRISM) is one of the methods used to overcome the drawbacks of the conventional RISM theory [43–46]. In this

*hagiwara@ccs.tsukuba.ac.jp

†otani@ccs.tsukuba.ac.jp

study, we combined DRISM with the ESM-RISM method to produce a more precise simulation method for the physical properties at the electrochemical interface. As a benchmark for the this new method, we calculated the electrochemical properties of the Pt(111)/aqueous HCl solution [HCl(aq)]. The potential of zero charges, standard hydrogen electrode potential, and grand-potential profiles as a function of the electrode potential and double-layer capacitances around the potential of zero charge were all successfully determined. The remainder of this paper is organized as follows. Section II provides details of a series of RISM based hybrid simulation methods. In Sec. III, we provide details of the computations. We then discuss the results of the benchmark calculations in Sec. IV. Finally, Sec. V provides a summary of the study.

II. METHOD

Here, we describe the theoretical details of a series of hybrid simulation methods using the RISM theory. Before detailed explanations, we provide a brief summary of the entire ESM-RISM (3D-RISM) framework. First, the one-dimensional RISM (1D-RISM) calculation with and without the dielectric correction is carried out to determine the isotropic bulk solution susceptibility, which is then used in ESM-RISM (3D-RISM). Here, 1D-RISM with and without the dielectric correction is denoted DRISM [43,44] and extended RISM (XRISM) [28–30], respectively. In ESM-RISM, the Laue-represented RISM (LRISM) equation requires the one-dimensional Fourier transform (1D-FT). However, the direct 1D-FT is a numerical instability due to the formulation of intramolecular correlation function. To overcome this problem, we introduce two approximation methods for 1D-FT of intramolecular correlation, i.e., Gaussian and damping schemes. The original ESM-RISM approach corresponds to XRISM with the Gaussian scheme [38]. Notably, in this paper, we introduce two methods due to different backgrounds: the dielectric correction is needed to recover the drawback of the XRISM theory, and the approximation of the 1D-FT method is due to the numerical problem in ESM-RISM. Hence, we first explain the 1D-RISM theory with and without dielectric correction. Then, we briefly introduce the 3D-RISM method and discuss ESM-RISM. Finally, we discuss the calculation method for the standard hydrogen electrode potential (SHE) measured from the absolute reference. In this study, we used the hartree atomic unit ($\hbar = e = m_e = 1$), unless otherwise specified.

A. 1D-RISM

First, we briefly discuss the XRISM theory developed by Hirata and Rossky. Since the original RISM theory is not suitable for the realistic solution consisting of dipolar molecules and ions, the XRISM theory via renormalizing the Coulomb potentials and introducing the appropriate closure relations was developed. The RISM equation takes the orientational average of multiple molecular sites and assumes that the correlation functions of a target solution depend only on the distance between the two molecular sites r . The total correlation function $h_{\alpha\gamma}$ and direct correlation function $c_{\alpha\gamma}$ between

the two sites are described by the following RISM equation:

$$\begin{aligned} \mathbf{h} &= \boldsymbol{\omega} * \mathbf{c} * \boldsymbol{\omega} + \boldsymbol{\omega} * \mathbf{c} * \boldsymbol{\rho} \mathbf{h} \\ &= [\mathbf{1} - \boldsymbol{\omega} * \mathbf{c} \boldsymbol{\rho}]^{-1} \boldsymbol{\omega} * \mathbf{c} * \boldsymbol{\omega}. \end{aligned} \quad (1)$$

Here, the Greek subscripts represent the atomic sites in all RISM components. ρ_α is the number density of RISM components, and asterisks indicate the convolution integral evaluated using the Fourier transform (FT) technique. $\omega_{\alpha\gamma}$ denotes the intramolecular correlation function. For the combination of α and γ in the same molecule, $\omega_{\alpha\gamma}$ is written in the Fourier space as follows:

$$\omega_{\alpha\gamma}(g) = \frac{\sin(g l_{\alpha\gamma})}{g l_{\alpha\gamma}}, \quad (2)$$

where $l_{\alpha\gamma}$ is the intramolecular distance between α and γ sites. When α and γ belong to different molecules, $\omega_{\alpha\gamma}$ is zero. The RISM equation contains two unknown quantities: $h_{\alpha\gamma}$ and $c_{\alpha\gamma}$. Therefore, the following closure equation was introduced to close the RISM equation:

$$g_{\alpha\gamma}(r) = \exp\{-\beta u_{\alpha\gamma}(r) + h_{\alpha\gamma}(r) - c_{\alpha\gamma}(r) + b_{\alpha\gamma}(r)\}, \quad (3)$$

where $g_{\alpha\gamma}(r)$ is a pair distribution function defined as $g_{\alpha\gamma}(r) = h_{\alpha\gamma}(r) + 1$ and $u_{\alpha\gamma}(r)$ is the pair potential represented by the sum of the van der Waals and electrostatic potentials. $\beta = 1/k_B T$, where k_B and T are Boltzmann coefficient and temperature, respectively. $b_{\alpha\gamma}(r)$ is a bridge function that includes higher-order effects, such as dipole-dipole interactions [47–50]. The hypernetted chain (HNC) closure is a popular form of closure equation [51,52],

$$g_{\alpha\gamma}(r) = \exp\{-\beta u_{\alpha\gamma}(r) + h_{\alpha\gamma}(r) - c_{\alpha\gamma}(r)\}, \quad (4)$$

where $b_{\alpha\gamma}(r)$ is neglected in Eqs. (3). The solution of the RISM equation was determined by numerically solving Eqs. (1) and (4). After convergence, we obtained the solution susceptibility $\chi_{\alpha\gamma}(g)$ as

$$\chi_{\alpha\gamma}(g) = \omega_{\alpha\gamma}(g) + \rho_\alpha h_{\alpha\gamma}(g). \quad (5)$$

$\chi_{\alpha\gamma}(g)$ appears in the first equality of Eq. (1), and we used $\chi_{\alpha\gamma}(g)$ to solve the 3D-RISM and LRISM equations, which are discussed in the following subsections.

Next, we describe DRISM introduced by Perkyns and Pettitt [43,44]. XRISM systematically underestimated the relative dielectric constant ϵ of solutions with dipolar molecules compared with the experimental values. For instance, ϵ of liquid water by XRISM is approximately 20, which is about four times smaller than the experiment ($\epsilon \sim 80$). This underestimation of ϵ is a systematic problem in XRISM for various water models as shown in Appendix A 1. This drawback originates from the renormalization of Coulomb potential in XRISM, which leads to overestimating the interionic correlation, and neglecting the bridge function, which includes the dipole-dipole interaction. To improve XRISM for finite-concentration solutions, the DRISM theory, which utilizes ϵ as an empirical parameter to screen the Coulomb interaction between charges in the solution, was developed. The dielectric correction was introduced into the RISM equation as follows:

$$\mathbf{h}' = [\mathbf{1} - \boldsymbol{\omega}' * \mathbf{c} \boldsymbol{\rho}]^{-1} \boldsymbol{\omega}' * \mathbf{c} * \boldsymbol{\omega}', \quad (6)$$

where $\mathbf{h}' = \mathbf{h} - \boldsymbol{\xi}$, $\boldsymbol{\omega}' = \boldsymbol{\omega} + \rho\boldsymbol{\xi}$, and $\boldsymbol{\xi}$ is a dielectric correction function (the details of $\boldsymbol{\xi}$ are also summarized in Appendix A 2). Owing to the simple modification of the RISM equation by DRISM, we obtained $\chi_{\alpha\gamma}(g)$ from Eq. (6) without any modifications to Eq. (5). Thus, the solution properties are improved by DRISM and are easily applied to 3D-RISM and ESM-RISM calculations via solution susceptibility.

Finally, we briefly discuss the recently developed XRISM with the new closure relation called XRISM-DB (DB: Dipole bridge) [50], which includes the dipole-dipole interactions as the bridge diagrams. Thus, the XRISM-DB method can reproduce the dielectric constant of the solution without phenomenological parameters in principle. However, it uses a parameter that reflects the effect of short-range correlation on the dipole-dipole interaction (B parameter), where the B parameter was self-consistently optimized. However, in the previous study, determining the B parameter utilizes the experimental dielectric constant. Thus, XRISM-DB requires us to develop the determination method for the B parameter without empirical parameters. In this study, as one of the simplest approaches, we consider the dielectric correction effect on the calculated physical properties at the electrochemical interface using DRISM combined with the ESM-RISM method.

B. 3D-RISM

3D-RISM is a hybrid simulation method that combines DFT and RISM [39,40]. The total energy functional of DFT, E_{DFT} , is replaced by the Helmholtz free energy, A , which can be written as

$$A = E_{\text{DFT}} + \Delta\mu_{\text{solv}}, \quad (7)$$

where $\Delta\mu_{\text{solv}}$ is the excess chemical potential. To obtain the distribution functions of the solutions, we solved the following 3D-RISM equation with the closure equation:

$$h_\gamma(\mathbf{r}) = \sum_\alpha \int d\mathbf{r}' c_\alpha(\mathbf{r}') \chi_{\alpha\gamma}(|\mathbf{r} - \mathbf{r}'|). \quad (8)$$

Here, α and γ represent the atomic sites of implicit and explicit solutions, respectively. The convolution in Eq. (8) can be solved in reciprocal space, in a manner similar to 1D-RISM. Thus, we solved the following RISM equation using the closure equation:

$$h_\gamma(\mathbf{g}) = \sum_\alpha c_\alpha(\mathbf{g}) \chi_{\alpha\gamma}(g), \quad (9)$$

where we determine $\chi_{\alpha\gamma}(g)$ by the result of the 1D-RISM calculation using Eq. (5), and the dielectric correction is applied to 3D-RISM via $\chi_{\alpha\gamma}(g)$ obtained by DRISM. The 3D-RISM method is formulated under canonical conditions. Thus, the total number of RISM particles is constant during the calculation, which is useful for evaluating the number of water molecules in layered materials [53–56].

C. ESM-RISM

The main idea of the ESM-RISM method is that the canonical condition of the electrons and RISM particles in 3D-RISM is extended to a grand-canonical ensemble using a mixed-boundary condition [38]. In the ESM-RISM, we

rewrite Eq. (9) using the Laue-represented form

$$h_\gamma(\mathbf{g}_\parallel, z) = \sum_\alpha \int dz' c_\alpha(\mathbf{g}_\parallel, z') \chi_{\alpha\gamma}(\mathbf{g}_\parallel, |z - z'|). \quad (10)$$

Here, $\chi_{\alpha\gamma}(\mathbf{g}_\parallel, |z - z'|)$ is obtained by $\chi_{\alpha\gamma}(g)$ discussed in Eq. (5) using inverse 1D-FT, which will be discussed later. In ESM-RISM, the dielectric correction is also due to the bulk solution susceptibility obtained by DRISM. The total energy function of the system is also described by the Helmholtz free energy, as shown in Eq. (7). By simultaneously solving the Kohn-Sham (KS) equation with ESM under the vacuum/slab/vacuum boundary condition [33] and the LRISM equation, we can treat both electrons and RISM particles under the grand-canonical condition. Thus, we can define the grand-potential Ω as

$$\Omega \equiv A - \mu_e(N - N_0) = A - \mu_e \Delta N. \quad (11)$$

Here, μ_e and ΔN indicate the electron chemical potential and difference in the total number of electrons between the charged and neutral systems, N and N_0 , respectively. Therefore, ESM-RISM can treat the formation mechanism of the EDL and the change in total energy by the excess charge without introducing a uniform background charge.

Numerically, to solve Eq. (10), we need to perform the inverse 1D-FT in the g_z direction for $\chi_{\alpha\gamma}(g)$ as follows:

$$\begin{aligned} \chi_{\alpha\gamma}(\mathbf{g}_\parallel, |z - z'|) &= \frac{1}{\pi} \int_0^\infty dg_z \chi_{\alpha\gamma}(g) \cos[g_z(z - z')] \\ &= \mathcal{F}_{g_z}^{-1}[\omega_{\alpha\gamma}(g)] + \rho_\alpha \mathcal{F}_{g_z}^{-1}[h_{\alpha\gamma}(g)]. \end{aligned} \quad (12)$$

Here, $\mathcal{F}_{g_z}^{-1}[f(g)]$ indicates the inverse 1D-FT in the g_z direction for a function $f(g)$; in the second equality, Eq. (5) was substituted into Eq. (12). We can easily perform a numerical integration in $\mathcal{F}_{g_z}^{-1}[h_{\alpha\gamma}(g)]$. However, because $\omega_{\alpha\gamma}(g)$ contains the delta function, direct evaluation of $\mathcal{F}_{g_z}^{-1}[\omega_{\alpha\gamma}(g)]$ provides only numerical noise. According to the original paper on ESM-RISM [38], to avoid numerical noise, the delta function of $\omega_{\alpha\gamma}$ is approximated by a Gaussian function with a width of κ , which is written as

$$\omega_{\alpha\gamma}(g) = \frac{\sin(g l_{\alpha\gamma})}{g l_{\alpha\gamma}} \exp(-g^2 \kappa^2 / 4). \quad (13)$$

Although this approximation allows us to carry out an analytical 1D-FT for the $\omega_{\alpha\gamma}(g)$ term, it causes a deviation in the results of 1D-RISM from the original implementation.

Here, we discuss another approximation of the first term in Eqs. (12), without any modifications to $\omega_{\alpha\gamma}(g)$ for the 1D-RISM. We performed numerical 1D-FT for $\omega_{\alpha\gamma}(g)$ under the finite integral range by introducing a damping function $W(g_z)$ as follows:

$$\begin{aligned} \mathcal{F}_{g_z}^{-1}[\omega_{\alpha\gamma}(g)] &= \frac{1}{\pi} \int_0^{g_{\text{cut}}} dg_z \omega_{\alpha\gamma}(g) \\ &\quad \times W(g_z) \cos[g_z(z - z')]. \end{aligned} \quad (14)$$

Here, g_{cut} is the cutoff radius of the reciprocal space. This technique is utilized in FT analysis for time-dependent dipole oscillation to obtain the optical absorption spectrum [57,58].

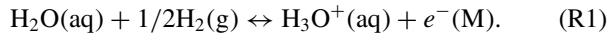
In this study, we used the explicit form of $W(g_z)$ as

$$W(g_z) = 1 - 3\left(\frac{g_z}{g_{\text{cut}}}\right)^2 + 2\left(\frac{g_z}{g_{\text{cut}}}\right)^3. \quad (15)$$

We defined g_{cut} as the cutoff radius of g in the 1D-RISM calculation. Using this approximation, we obtained $\chi_{\alpha\gamma}(\mathbf{g}_{\parallel}, |z - z'|)$ without modifying the results of the 1D-RISM. In this study, we also compared the results of ESM-RISM with a Gaussian function to those with a damping function. Hereafter, the former and latter methods are termed as ‘‘Gaussian’’ and ‘‘damping’’ schemes, respectively. Further detailed numerical techniques used in the ESM-RISM are described in Appendices B–E.

D. SHE potential

Here, we briefly discuss the calculation method for SHE potential using ESM-RISM, as discussed by Haruyama *et al.* [59]. The SHE is one of the most fundamental reference electrodes for determining the electrode potential at the aqueous interface due to an electrochemically stable reaction. The equilibrium reaction for SHE is the hydrogen evolution reaction, which is expressed as



To determine the SHE potential, we calculated the change in Gibbs free energy ΔG_{SHE} for reaction R1 by

$$\Delta G_{\text{SHE}} = G\{\text{H}_2\text{O}(\text{aq})\} + 1/2G\{\text{H}_2(\text{gas})\} - G\{\text{H}_3\text{O}^+(\text{aq})\}, \quad (16)$$

where each component is defined on the right-hand side as follows:

$$\begin{aligned} G\{\text{H}_2\text{O}(\text{aq})\} &= A\{\text{H}_2\text{O}(\text{aq})\} + E_{\text{ZP}}(\text{H}_2\text{O}), \\ G\{\text{H}_2(\text{gas})\} &= A\{\text{H}_2(\text{gas})\} + E_{\text{ZP}}(\text{H}_2), \\ G\{\text{H}_3\text{O}^+(\text{aq})\} &= A\{\text{H}_3\text{O}^+(\text{aq})\} + E_{\text{ZP}}(\text{H}_3\text{O}^+). \end{aligned}$$

Here, $A\{\text{H}_2(\text{gas})\}$ is the sum of $E_{\text{DFT}}\{\text{H}_2(\text{gas})\}$ and $-TS$, where S is the standard molar entropy term obtained from the NIST-JANAF thermodynamic table [60]. E_{ZP} is the zero-point vibration energy in the gas-phase molecules, the values of which can be found elsewhere [59,61]. Then, we obtained the SHE potential U_{SHE} using the following electromotive force formula:

$$U_{\text{SHE}} = -\Delta G_{\text{SHE}}/nF, \quad (17)$$

where n and F indicate the number of reacted electrons and the Faraday constant, respectively. According to the discussion by Haruyama *et al.*, the reference potential of U_{SHE} by ESM-RISM is set to the inner potential Φ_{S} , which is a potential in the bulk solution [59]. In addition, we can use U_{SHE} vs Φ_{S} as the reference potential for an electrode potential determined by ESM-RISM with the same solution parameter as follows [62,63]:

$$U [\text{vs SHE}] = U [\text{vs } \Phi_{\text{S}}] - U_{\text{SHE}} [\text{vs } \Phi_{\text{S}}]. \quad (18)$$

In this study, we used this relationship to determine the potential of zero charge (PZC), U_{PZC} , measured from U_{SHE} .

III. COMPUTATIONAL DETAILS

All calculations were performed using the Quantum ESPRESSO package [66,67] within a framework of plane-wave basis sets and ultrasoft pseudopotential [68–70]. The cutoff energies for the wave function, and augmented charge, were 40 and 320 Ry, respectively. \mathbf{k} -point samplings of $4 \times 4 \times 1$ and only the Γ point were employed for the surface and isolated systems, respectively. We used the spin-unpolarized generalized gradient approximation [71] for the exchange-correlation energy functional with a nonlinear core correction [72]. The Pt(111) surface was represented using a repeated slab model with three atomic layers. For constructing the Pt(111) slab, the experimental lattice constant of 3.925 Å of face-centered-cubic Pt was employed [73]. In the electrode calculations, the atomic positions were fixed. For isolated H_2 and H_2O molecules in a vacuum, we used a unit cell with a size of $20 \times 20 \times 20 \text{ \AA}^3$. For the molecular system, we performed geometry optimization until the forces acting on the atoms became smaller than 10^{-3} Ry/bohr. In the free energy calculation for hydrogen-bonded molecules, we calculated E_{ZP} for the molecules in the gas phase at the BLYP/6-311+G(3df, 2pd) level using the Gaussian16 package [74].

For the ESM-RISM calculations, we used HCl(aq) with an electrolyte concentration of one molar [1M-HCl(aq)] as the standard electrolyte solution. The cutoff energy for the correlation functions was 160 Ry, and the temperature parameter of the RISM solution was 300 K. The iterative calculation for determining the correlation functions was accelerated by the modified direct inversion of the iterative subspace (MDIIS) method, in which the criterion for the root mean square of the residual for the total correlation function was 1.0×10^{-6} [75]. We adopted the Kovalenko and Hirata type of closure function [39], and the solvation free energy was determined using the Gaussian fluctuation model [76]. The cells calculated for the ESM-RISM calculations are shown in Figs. 1(a)–1(c). For the Pt(111)/1M-HCl(aq) interface, we used a half-cell model with the vacuum/slab/solution (VSS) boundary condition. We employed solution/ion/solution boundary conditions for the hydrated ions and molecules.

For the 1D-RISM calculation, the real-space and reciprocal-space cutoff radii were 999.8 bohrs and 18.763 bohr^{-1} with 5973 grid points, respectively. The convergence criterion for the MDIIS in 1D-RISM was 1.0×10^{-8} . In the DRISM calculation, we used $\varepsilon = 78.4$, as in a previous study [45]. For the Gaussian scheme, we set κ in Eqs. (13) to 0.3162 bohrs. To represent the van der Waals interactions, we employed the 12-6 type of Lennard-Jones (LJ) potential. The LJ parameters for the different atom types were constructed using the Lorentz-Berthelot combination rule [77,78]. For implicit and explicit water molecules, we used the extended simple point charge (cSPC/E) model [79]. The LJ parameters for the Na^+ and Cl^- ions were obtained from Ref. [80]. For an implicit H_3O^+ ion, we employed the LJ and charge parameters optimized by Bonthuis *et al.* [81], where we modified the LJ parameters for the H site to $\varepsilon_{\text{H}} = 0.046 \text{ kcal/mol}$ and $\sigma_{\text{H}} = 0.6 \text{ \AA}$. For explicit Pt atoms, we employed the LJ parameter used by Haruyama *et al.* [59].

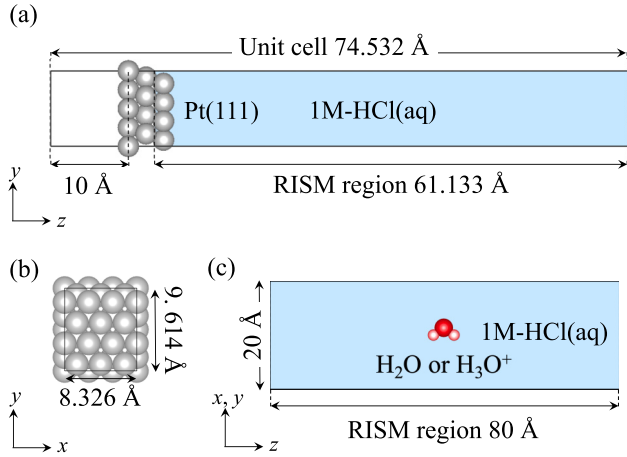


FIG. 1. Calculation cells for (a) the Pt(111) electrode/1M-HCl(aq) interface with the vacuum/slab/solution boundary condition and (c) a H₂O or H₃O⁺ in 1M-HCl(aq) with the solution/ion/solution boundary condition. (b) Top view of the calculation cell for the Pt(111) surface. Gray, pink, and red balls represent Pt, H, and O atoms, respectively. All the atomic geometries are visualized by VESTA program [64,65].

IV. RESULTS AND DISCUSSION

In this section, we discuss the results of the ESM-RISM method with and without the dielectric correction. First, as a benchmark of DRISM, we briefly compare the results of the mean activity coefficients between XRISM and DRISM within the 1D-RISM framework using an aqueous NaCl solution [NaCl(aq)]. Second, we discuss the hydration free energy of a water molecule. Then, the PZC results and the absolute SHE potential at the clean Pt(111) electrode are discussed. Finally, we discuss the results of the grand-potential profiles and double-layer capacitance at the Pt(111)/1M-HCl(aq) interface.

A. Check the implementation of DRISM

First, we verified the implementation of DRISM within the 1D-RISM framework. For this purpose, we calculated the mean activity coefficient of the solute ions in NaCl(aq) with a molar concentration m , $\gamma_{m,\pm}$, which can be observed experimentally. $\gamma_{m,\pm}$ can be defined as the difference in the excess chemical potential $\Delta\mu_{\text{ex}}$ between the aqueous solution with a finite electrolyte concentration and the infinite dilution system as follows:

$$\nu k_{\text{B}}T \ln \gamma_{m,\pm} = k_{\text{B}}T \ln \frac{\rho_{\text{w}}}{\rho_{\text{w},\infty}} + \sum_i s_i \Delta\mu_{\text{ex},i}. \quad (19)$$

Here, subscript i indicates the ionic species of the solute. For the NaCl, $s_i = 1$, and $\nu = \sum_i s_i = 2$. ρ_{w} and $\rho_{\text{w},\infty}$ are the numbers of water molecules for the actual and infinite dilution systems, respectively. Further derivations of $\gamma_{m,\pm}$ can be found elsewhere [45,46].

The results for $\gamma_{m,\pm}$ are shown in Fig. 2, where we also calculated $\gamma_{m,\pm}$ using 1D-RISM with the Gaussian scheme. We found that XRISM significantly underestimates $\gamma_{m,\pm}$ com-

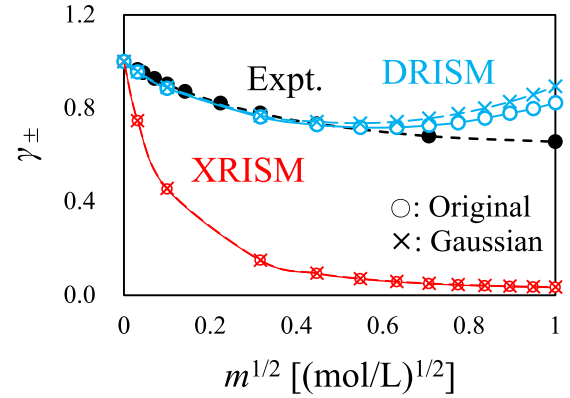


FIG. 2. Mean activity coefficients for NaCl(aq) γ_{\pm} as a function of square root of ion concentrations $m^{1/2}$. Red and blue colors denote XRISM and DRISM, respectively. Open circles and cross symbols denote the results obtained by the original implementation of 1D-RISM using Eq. (2) and 1D-RISM with the Gaussian scheme discussed in Eq. (13). Black circles are experimental data obtained from Ref. [82].

pared to the experiment [82], which is a well-known drawback of the XRISM theory. After dielectric correction, the results of $\gamma_{m,\pm}$ by DRISM reproduce the experimental results well. This trend is consistent with previous results for 1D-RISM [45,46], and thus, we confirm the successful implementation of DRISM. This is a strong example of the importance of the dielectric correction in the RISM theory, where the DRISM theory improves bulk solution properties for both original and Gaussian smeared $\omega_{\alpha\gamma}$. Moreover, we briefly compare the Gaussian smearing effect on $\omega_{\alpha\gamma}$ discussed in Eq. (13) into the original implementation using Eqs. (2). XRISM with the Gaussian scheme agrees well with the original XRISM data. By contrast, for DRISM, the Gaussian scheme overestimates $\gamma_{m,\pm}$ compared to the original scheme. Therefore, the dielectric correction effect in the 1D-RISM framework is enhanced in the Gaussian scheme. For simplicity, in the following sections, we call the results of the ESM-RISM (3D-RISM) with and without the dielectric correction as “DRISM” and “XRISM” unless otherwise specified.

B. Hydration free energy

Here, we briefly discuss the results of the hydration free energy ΔG_{hyd} obtained using ESM-RISM. First, we discuss the effect of DRISM on ΔG_{hyd} and then compare ΔG_{hyd} obtained by ESM-RISM to that obtained by 3D-RISM. ΔG_{hyd} is defined as

$$\Delta G_{\text{hyd}} = A\{\text{H}_2\text{O}(\text{aq})\} - E_{\text{DFT}}\{\text{H}_2\text{O}(\text{gas})\},$$

where $A\{\text{H}_2\text{O}(\text{aq})\}$ and $E_{\text{DFT}}\{\text{H}_2\text{O}(\text{gas})\}$ represent the Helmholtz free energy of a water molecule in aqueous solution and the DFT total energy for the isolated H₂O molecule, respectively.

Figure 3(a) shows the results for ΔG_{hyd} , where liquid water is used as the aqueous solution. For both the Gaussian and damping schemes, the results of ΔG_{hyd} obtained by DRISM were lower than those obtained by XRISM. This result was due to the difference in the dielectric constant of liquid water.

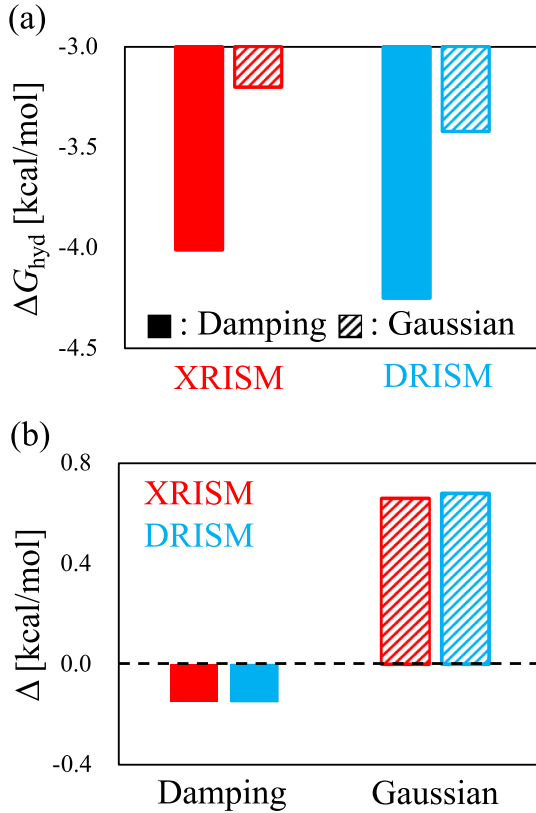


FIG. 3. (a) Comparison of the hydration free energies ΔG_{hyd} between XRISM and DRISM. Here, we also show ΔG_{hyd} obtained by the damping and Gaussian schemes. (b) Free energy differences between ESM-RISM and 3D-RISM Δ . The red and blue bars indicate XRISM and DRISM, respectively. The filled and striped bars denote the damping and Gaussian schemes, respectively.

However, ΔG_{hyd} by DRISM is a still higher value comparing to the experimental value of ΔG_{hyd} that is -6.3 kcal/mol (23.06 kcal/mol = 1 eV) [83]. Thus, although this result overestimates ΔG_{hyd} compared with the experiment, DRISM slightly improves ΔG_{hyd} . Because ΔG_{hyd} depends on the implicit water model [84], to reproduce experimental ΔG_{hyd} , we need to tune the model of the implicit water molecule. However, we used the present implicit water model throughout this study for the following reasons: our focus is the dielectric correction effect on the calculated properties, and underestimation of ϵ is a systematic problem in the XRISM theory.

Then, we checked the accuracy of real-space convolution in Eq. (10) by comparing ΔG_{hyd} between the ESM-RISM and 3D-RISM. Note that we used the same computational conditions for 3D-RISM as explained in Sec. II. Because the ESM-RISM method utilizes $\chi_{\alpha\gamma}$ as in 3D-RISM, ideally, ΔG_{hyd} by ESM-RISM converges to that by 3D-RISM. Therefore, we defined the difference in ΔG_{hyd} (Δ) between the ESM-RISM and 3D-RISM methods as follows:

$$\Delta = \Delta G_{\text{hyd}}^{\text{ESM-RISM}} - \Delta G_{\text{hyd}}^{\text{3D-RISM}},$$

where $\Delta G_{\text{hyd}}^{\text{ESM-RISM}}$ and $\Delta G_{\text{hyd}}^{\text{3D-RISM}}$ indicate ΔG_{hyd} obtained by ESM-RISM and 3D-RISM, respectively. Figure 3(b) shows the results of Δ , and we found that the absolute values of Δ

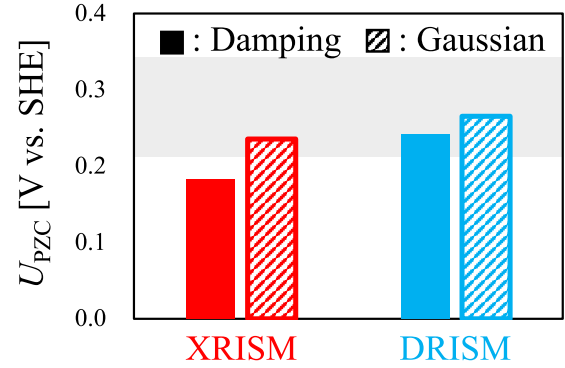


FIG. 4. Potential of zero charge U_{PZC} measured from the SHE potential at the Pt(111)/1M-HCl(aq) interface. Gray shaded area indicates the experimental PZC range for the Pt(111) electrode. The red and blue bars indicate XRISM and DRISM, respectively. The filled and striped bars denote the damping and Gaussian schemes, respectively.

obtained by the damping scheme are smaller than those of the Gaussian. Thus, the damping scheme tends to reproduce $\chi_{\alpha\gamma}$ used in 3D-RISM compared to the Gaussian. In addition, we do not find a difference in Δ between XRISM and DRISM, which indicates that the origin of Δ comes mainly from the approximation for constructing $\chi_{\alpha\gamma}(\mathbf{g}_{\parallel}, |z - z'|)$. Therefore, we consider the damping scheme to be a better approximation than the Gaussian scheme. Hereinafter, we mainly discuss the results of the damping scheme unless otherwise specified and present the results of the Gaussian scheme as a reference of the conventional implementation.

C. PZC and absolute SHE potential

Here, we first discuss the PZC results at the Pt(111)/1M-HCl(aq) interface. We determine U_{PZC} versus Φ_{S} using μ_e of the Pt(111) electrode without excess surface charges (μ_{PZC}) measured from the Φ_{S} level, which can be written as

$$U_{\text{PZC}} [\text{vs } \Phi_{\text{S}}] = -\mu_{\text{PZC}}/e [\text{vs } \Phi_{\text{S}}],$$

where e denotes elemental charge. Because ϵ_{F} corresponds to the energy variation owing to the change in the number of electrons, μ_e measured from Φ_{S} must satisfy

$$\mu_e = \epsilon_{\text{F}} - \Phi_{\text{S}} = \partial A / \partial N. \quad (20)$$

In ordinal DFT, the first equality in Eq. (21) is guaranteed by the Janak theorem [85]. We provide the proof of the Janak theorem within the 3D-RISM and ESM-RISM frameworks in Appendix F.

The results for U_{PZC} vs SHE are shown in Fig. 4, where the reference electrode potential was converted using Eq. (19). U_{PZC} obtained by DRISM was higher than that obtained using XRISM. Previously, U_{PZC} at the Pt(111)/aqueous solution interface was observed with a range from 0.23 [86] to 0.36 V vs SHE [87]. Note that the previous experiments used the HClO_4 salt instead of HCl to avoid the specific adsorption of Cl^- , which affects the PZC potentials and double-layer capacitance C_{dl} (C_{dl} will be discussed later) [88]. Since we do not consider the specific adsorption in this paper due to the implicit treatment of Cl^- , we might compare the present results to the

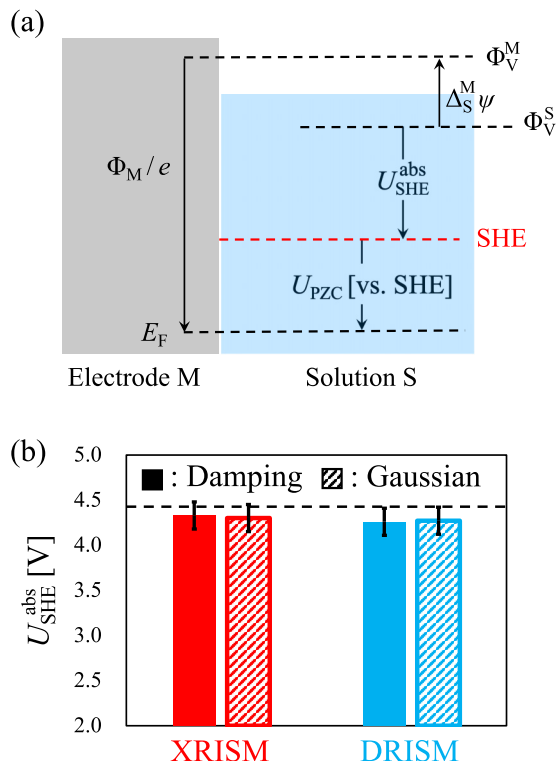


FIG. 5. (a) Schematic potential path for the absolute SHE potential U_{SHE}^{abs} . Φ_V^M and Φ_V^S denote the vacuum level close to the surface of the electrode M and the solution S, respectively. The latter vacuum level is called outer potential [59]. (b) U_{SHE}^{abs} calculated by ESM-RISM. Horizontal dashed line denotes the experimental value of U_{SHE}^{abs} determined to be 4.44 V by Trasatti [89]. Error bars come from the range of $\Delta_S^M \psi$. The red and blue bars indicate XRISM and DRISM, respectively. The filled and striped bars denote the damping and Gaussian schemes, respectively.

experiment. We found that XRISM slightly underestimated U_{PZC} compared with the experimental range. However, after dielectric correction, U_{PZC} is in reasonable agreement with the lower bound of the experimental range. Thus, DRISM with the damping scheme improves not only the bulk solution properties but also the PZC potential at the electrochemical interface.

Before discussing the results of the SHE potential, we briefly explain the calculation method for the absolute SHE potential U_{SHE}^{abs} . Because the inner potential cannot be the universal reference potential [59,61], to compare the U_{SHE} between the different methods, we converted U_{SHE} from Φ_S to the absolute SHE potential. According to the discussions by Trasatti, the absolute electrode potential corresponds to the work function Φ_M of metals in aqueous solutions [89,90]. Figure 5(a) shows the potential path for calculating the absolute SHE potential proposed by Trasatti. U_{SHE}^{abs} can be determined by Φ_M , the contact (or Volta) potential difference $\Delta_S^M \psi$, and U_{PZC} vs SHE using the following relation:

$$U_{SHE}^{abs} = \Phi_M/e + \Delta_S^M \psi - U_{PZC} [vs SHE]. \quad (21)$$

By Eq. (22), Trasatti experimentally obtained $U_{SHE}^{abs} = 4.44$ V with an Hg electrode, whose value is recommended by

the International Union of Pure and Applied Chemistry (IUPAC) [91].

We determined U_{SHE}^{abs} using the calculated $\Phi_M = 5.76$ eV for the three-layered Pt(111) slab and $\Delta_S^M \psi = 1.1 \sim 1.4$ V obtained from first-principles calculations by Otani *et al.* [5]. Figure 5(b) presents the results for U_{SHE}^{abs} . All the results are very close to each other, and the central values of U_{SHE}^{abs} obtained by XRISM and DRISM are 4.33 and 4.27 V, respectively. These values agree well with U_{SHE}^{abs} obtained by Trasatti [89]. However, we found that the results for U_{SHE}^{abs} obtained using DRISM were slightly lower than those obtained using XRISM. This tendency arises from the results of U_{PZC} vs SHE, because the potential conversion using Eq. (22) considers U_{PZC} . Note that to obtain a reasonable U_{PZC} vs SHE, we also need to determine the precise U_{SHE} vs Φ_S , which comes from the bulk solution properties, as discussed in Sec. IID. Thus, to consider the absolute SHE potential, we must consider both the bulk solution properties of the reactants and the electrode potential at the electrochemical interface.

D. Grand-potential profile and double-layer capacitance

Here, we show the results of the grand-potential profiles $\Delta\Omega$ as a function of the electrode potential U vs U_{PZC} and C_{dl} , which originates from the formation of an EDL at the Pt(111)/1M-HCl(aq) interface. Figure 6(a) shows the results of $\Delta\Omega$, which were obtained by introducing an excess charge ΔN to the electrode surface. ΔN changed from -1.0 e/cell to $+1.0$ e/cell at 0.05 e/cell intervals. The $\Delta\Omega$ profile shows the approximate inverse of the parabolic shape centered at U_{PZC} . This result is consistent with the constant-capacitance model explained by the Lippmann equation for an ideal electrode [92,93], and the curvature of $\Delta\Omega$ corresponds to the double-layer capacitance C_{dl} . To determine the constant term of C_{dl} around U_{PZC} , we used the third-order polynomial fitting method proposed in Ref. 62. The fitted $\Delta\Omega$ profiles are shown as solid curves in Fig. 6(a), and C_{dl} around U_{PZC} corresponds to the fitting coefficient of the second-order polynomial function.

The results for C_{dl} obtained by polynomial fitting are shown in Fig. 6(b), and C_{dl} obtained by DRISM was slightly larger than that obtained by XRISM. The results of C_{dl} obtained by DRISM are in reasonable agreement with the typical value of the observed double-layer capacitance shown by the broken line [87]. Furthermore, C_{dl} obtained using the Gaussian scheme tends to be larger than that obtained using the damping scheme, and thus the Gaussian overestimates C_{dl} compared to the experimental value. We will discuss later further comparison of C_{dl} between the present and recent experimental studies.

To interpret the dependence of C_{dl} on the choice of the methods, we carried out further analysis using an idea of the contact layer in the Helmholtz layer of EDL. According to Ando *et al.* [7] and co-workers [54], C_{dl} can be divided into contact layer and water layer contributions, which can be written as

$$C_{dl} = \frac{4\pi S}{\lambda}, \quad (22)$$

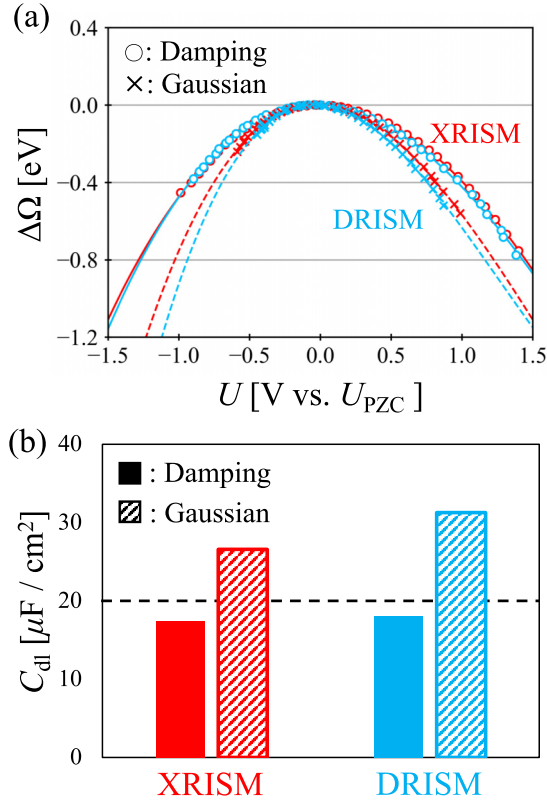


FIG. 6. (a) Change in the grand potential $\Delta\Omega$ as a function of the electrode potential U vs U_{PZC} . The open circles and crosses denote the damping and Gaussian schemes, respectively. Solid curves are fitted data of $\Delta\Omega$ with the third order of the polynomial function. (b) Double-layer capacitance C_{dl} around U_{PZC} as well as the experimental data [87] presented by a horizontal dashed line. The filled and striped bars denote the damping and Gaussian schemes, respectively. The red and blue colors indicate XRISM and DRISM, respectively.

where S is the surface area and

$$\lambda = l_c/\epsilon_c + l_w/\epsilon_w. \quad (23)$$

Here, l_c (ϵ_c) is the thickness (dielectric constant) of the contact layer, and l_w (ϵ_w) is the screening length (dielectric constant) of the water. The magnitude of ϵ_c is at most a few times higher than the permittivity of a vacuum because there are no screening media at the contact layer [7]. According to the theory of EDL, the typical length of l_w is estimated to be a several Å. As the typical value of ϵ_w is approximately 80, λ can be approximated as l_c/ϵ_c . Therefore, we consider that the tendency of C_{dl} shown in Fig. 6(b) can be explained by the thickness of the contact layer. To prove this concept, we must define the thickness of the contact layer within the ESM-RISM framework.

Recently, Shimada *et al.* analyzed the double layer at an MXene surface with various surface terminations using ESM-RISM [42] and proposed the definition of the double layer. Figure 7(a) shows the laterally averaged charge density distributions $\Delta\tilde{\sigma}(z)$ for the excess surface electrons and induced RISM charges from the PZC [$\Delta\tilde{\sigma}_{ele}(z)$ and $\Delta\tilde{\sigma}_{sol}(z)$] at an excess charge of $10.0 \mu\text{C}/\text{cm}^2$. Here, we show the result of DRISM with the damping scheme as a representative, and

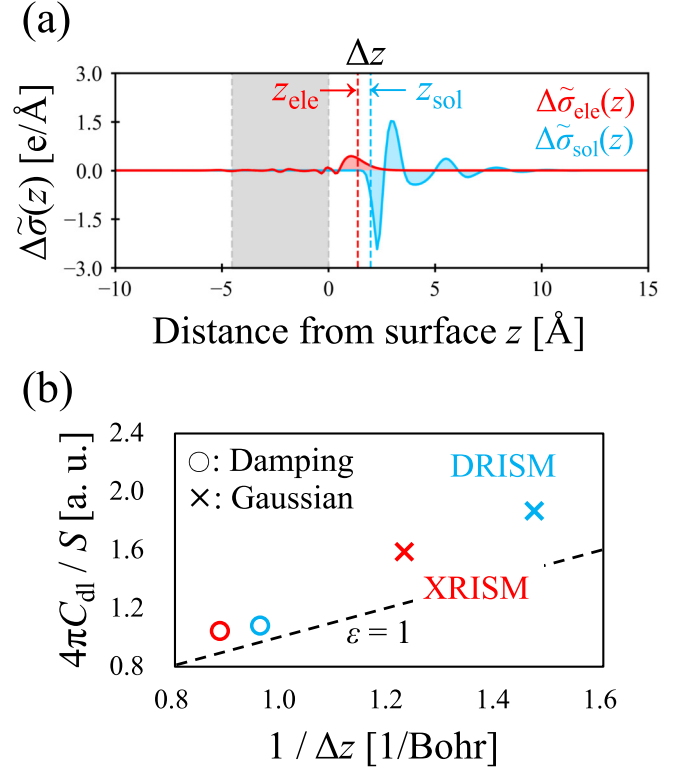


FIG. 7. (a) Laterally averaged charge density distributions for excess electrons and a RISM solution [$\Delta\tilde{\sigma}_{ele}(z)$ and $\Delta\tilde{\sigma}_{sol}(z)$] obtained by DRISM using the damping scheme with excess surface charge of $10.0 \mu\text{C}/\text{cm}^2$. The red and blue filled curves represent $\Delta\tilde{\sigma}_{ele}(z)$ and $\Delta\tilde{\sigma}_{sol}(z)$, respectively. The red and blue vertical dashed lines indicate the positions of effective charge planes (see text) for $\Delta\tilde{\sigma}_{ele}(z)$ and $\Delta\tilde{\sigma}_{sol}(z)$, respectively. The gray shaded area indicates the slab region. (b) Correlation between $4\pi C_{dl}/S$ and $1/\Delta z$. The red and blue symbols denote XRISM and DRISM, respectively. The open circles and cross symbols denote the damping and Gaussian schemes, respectively. The dashed line indicates the dielectric constant assumed to be 1 for a guide for the eye.

there are no qualitative differences in the charge densities between XRISM and DRISM. From this image of $\Delta\tilde{\sigma}(z)$, we define the thickness of the contact layer Δz as the distance of effective charge planes between $\Delta\tilde{\sigma}_{ele}(z)$ and $\Delta\tilde{\sigma}_{sol}(z)$ (z_{ele} and z_{sol}). z_{ele} and z_{sol} are defined as follows:

$$z_{ele} = \frac{\int_{-\infty}^{\infty} z \Delta\tilde{\sigma}_{ele}(z) dz}{\int_{-\infty}^{\infty} \Delta\tilde{\sigma}_{ele}(z) dz}, \quad (24)$$

$$z_{sol} = \frac{\int_{-\infty}^{\infty} z \Delta\tilde{\sigma}_{sol}(z) dz}{\int_{-\infty}^{\infty} \Delta\tilde{\sigma}_{sol}(z) dz}, \quad (25)$$

$$\Delta z = z_{sol} - z_{ele}. \quad (26)$$

Here, we define the outermost layer of the Pt atom position on the solution side as the origin of the z axis. Interestingly, this is very close to the definition of an effective image plane on the jellium surface used by Lang and Kohn [94].

We now discuss the correlation between C_{dl} and the inverse of Δz as shown in Fig. 7(b). We found that C_{dl} correlated well with $1/\Delta z$, and its slope corresponding to ϵ_c was close to 1. This result is consistent with ϵ_c estimated by Ando *et al.*, and we consider that C_{dl} mainly arises from the thickness

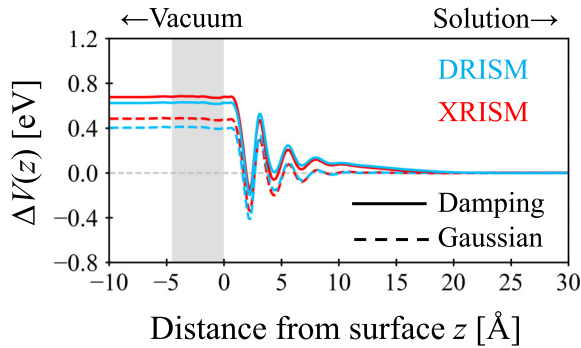


FIG. 8. Laterally averaged induced potential $\Delta V(z)$ by excess surface charge of $10.0 \mu\text{C}/\text{cm}^2$. The gray shaded area indicates the slab region. The red and blue lines denote XRISM and DRISM, respectively, and the solid and dashed lines denote the damping and Gaussian schemes, respectively.

of the contact layer defined by the interfacial charge distributions. The Gaussian scheme systematically underestimates Δz , which might be due to the broadened intramolecular correlation function, and the damping scheme can overcome the drawback of the Gaussian. In addition to the approximation of the convolution integral, dielectric correction further improved Δz . Therefore, DRISM with the damping scheme developed here well describes the C_{dl} and thickness of the contact layer at the Pt(111)/1M-HCl(aq) interface owing to the improved solution susceptibility. Figure 8 shows the results of the laterally averaged induced potential $\Delta V(z)$ by excess surface charge. Flat potentials from the surface slab to the vacuum region correspond to the electrode potential at the excess surface charge of $10.0 \mu\text{C}/\text{cm}^2$ measured from the bulk solution potential. The induced electrode potential by DRISM is lower than that by XRISM. The electrode potential is proportional to the inverse of C_{dl} , which relates with the curvature of grand-potential profile shown in Fig. 6(a), and the result of the induced electrode potential is consistent with the order of C_{dl} shown in Fig. 7(b). Thus, this result indicates that C_{dl} plays a role to determine the electrode potential. Hence, we expect that the dielectric correction with the damping scheme improves the relationship between the excess surface charge and surface electrode potential, which plays a significant role in theoretically elucidating the electrochemical reaction at the electrode/electrolyte solution interface.

Here, we briefly compare the result of C_{dl} to the more recent experiments. Recent electrochemical measurement shows a huge C_{dl} of about $100 \mu\text{F}/\text{cm}^2$ around the PZC level, which is larger than the present result of C_{dl} , at the interface between the dilute concentration aqueous electrolyte solution (about a few mmol/L) and the Pt(111) electrode [95,96]. The model analysis on EDL by Ojha *et al.* shows that the huge C_{dl} comes from the ion-surface attractive interaction and chemisorbed water. The ESM-RISM method takes account of the former picture via the electrostatic interaction between explicit and implicit particles. In contrast, we do not include the latter effect, because the implicit water model does not describe electron transfer between the water and electrode. Thus, the present result of C_{dl} captures the dielectric response of liquid water and the presence of the contact layer without

the chemisorbed water. Within the ESM-RISM framework, to improve the description of the electrode/water interface, we need to introduce chemisorbed water molecules as explicit particles.

V. SUMMARY

In this study, we implemented the DRISM method into the ESM-RISM framework and proposed an approximation method to evaluate the LRISM equation called the damping scheme. As a benchmark test for DRISM, we calculated the concentration dependence of the mean activity coefficient for NaCl(aq). We confirmed the successful implementation of the DRISM method, which reproduced the experimental data well. In addition, we found overworking of the dielectric correction for the intramolecular correlation function with Gaussian smearing. Then, we calculated the hydration free energy of neat water. The result obtained by DRISM and the damping scheme is in reasonable agreement with that obtained by 3D-RISM. After the above benchmarks, we applied the developed method to a Pt(111)/1M-HCl(aq) interface. The results of the electrochemical properties at the interface, such as PZC, absolute SHE potential, and double-layer capacitance, reasonably agree with the previous experiments. In addition, an almost linear correlation between the double-layer capacitance and the inverse of the contact-layer thickness was found. This result suggests the importance of the contact layer when considering the properties of the electric double layer. We found that the dielectric corrected ESM-RISM with a damping scheme improves not only bulk solution properties but also the electrified interface properties via the improved solution susceptibility. We believe that the present method will be a useful tool for revealing the physical properties of electrochemical interfaces.

ACKNOWLEDGMENTS

S.H. and M.O. acknowledge Dr. Takenaka and Dr. Shimada for their valuable comments on ESM-RISM calculations. This work was supported by MEXT as the ‘‘Program for Promoting Research on the Supercomputer Fugaku’’ (Fugaku Battery & Fuel Cell Project), Grant No. JPMXP1020200301. This study was also supported by JSPS KAKENHI (Grants No. JP22K14643 and No. JP20H05673). Parallel computations were performed using the Fugaku supercomputer provided by the RIKEN Center for Computational Science (Project IDs: hp200131, hp210173, hp220088)/FLOW provided by Nagoya University. We also used the computational resources of the supercomputer at the Institute for Solid State Physics at the University of Tokyo.

APPENDIX A: DIELECTRIC CORRECTION IN 1D-RISM

1. Dielectric constant in XRISM for typical water models

XRISM with the conventional closures such as HNC and KH gives a trivial ϵ for noninteracting dipolar gas, which is obtained by

$$\epsilon = 1 + 3y, \quad (\text{A1})$$

TABLE I. Dielectric constants ε in the XRISM calculation for typical water models, as well as μ and charges on H, O, and lone-pair sites (Q_H , Q_O , and Q_L). Further details for the water models are discussed in the previous studies [59,79].

Water model	Q_H (e)	Q_O (e)	Q_L (e)	μ (debyes)	ε
SPC	0.41	0.82		2.27	18.59
SPC/E	0.4238	-0.8476		2.35	19.79
TIP3P	0.417	-0.834		2.35	19.74
TIP5P	2.41	0.00	-2.41	2.29	18.87

where $y = 4\pi\rho_{\text{pol}}\mu^2\beta/9$ denotes the dipole density. ρ_{pol} and μ are the number density of the polar molecules and the strength of the dipole moment per polar molecule along the z axis, respectively. For the liquid water, ρ_{pol} is calculated by the liquid water concentration (1 g/cm³), and μ depends on the water models. Table I shows ε in XRISM calculated for typical water models, and we clearly see that XRISM systematically underestimates ε compared to the experimental value ($\varepsilon \sim 80$). Thus, we need to consider the dielectric correction for more precise calculations.

2. Dielectric correction function

Here, we briefly introduce the expression for the dielectric correction term $\xi_{\alpha\gamma}(g)$ in DRISM. The derivatives of $\xi_{\alpha\gamma}(g)$ can be found in Ref. [43]. $\xi_{\alpha\gamma}(g)$ has a nonzero value when the combination of α and γ is the intra-atomic site of the polar molecule, which can be written as

$$\xi_{\alpha\gamma}(g) = j_0(gd_{\alpha x})j_0(gd_{\alpha y})j_1(gd_{\alpha z}) \times \tilde{h}(g)j_0(gd_{\gamma x})j_0(gd_{\gamma y})j_1(gd_{\gamma z}), \quad (\text{A2})$$

where j_0 and j_1 are the zeroth- and first-order spherical Bessel functions, respectively. By contrast, when the combination of α and γ is an interatomic site or each ion, $\xi_{\alpha\gamma}(g)$ is zero. $d_{\alpha i}$ ($i = x, y, z$) represents the atomic position in a polar molecule measured from the center of the absolute charges. The kernel $\tilde{h}(g)$ is defined as

$$\tilde{h}(g) = \frac{1}{\rho_{\text{tot}}} \left(\frac{\varepsilon - 1}{y} - 3 \right) \exp(-a^2g^2/4), \quad (\text{A3})$$

where ρ_{tot} denotes the total number density of the solution. For the a parameter, 0.5 Å is typically used for aqueous solutions.

APPENDIX B: SEPARATION OF DIRECT CORRELATION FUNCTION

In the practical 3D-RISM (and 1D-RISM) calculation, for numerical stability, c_α is divided into short- and long-range contributions, which can be written in real space as

$$c_\alpha(\mathbf{r}) = c_\alpha^S(\mathbf{r}) + c_\alpha^L(\mathbf{r}). \quad (\text{B1})$$

Here, superscripts ‘‘S’’ and ‘‘L’’ denote short- and long-range contributions, respectively. We employed $c_\alpha^L(\mathbf{r}) = -\beta u_\alpha^L(\mathbf{r})$, which is the asymptotic behavior of $\lim_{r \rightarrow \infty} c_\alpha(\mathbf{r})$. In 3D-RISM, $u_\alpha^L(\mathbf{r})$ is calculated in reciprocal space and expressed as

$$u_\alpha^L(\mathbf{g}) = -q_\alpha v_{\text{DFT}}(\mathbf{g}) \exp(-g^2\tau^2/4), \quad (\text{B2})$$

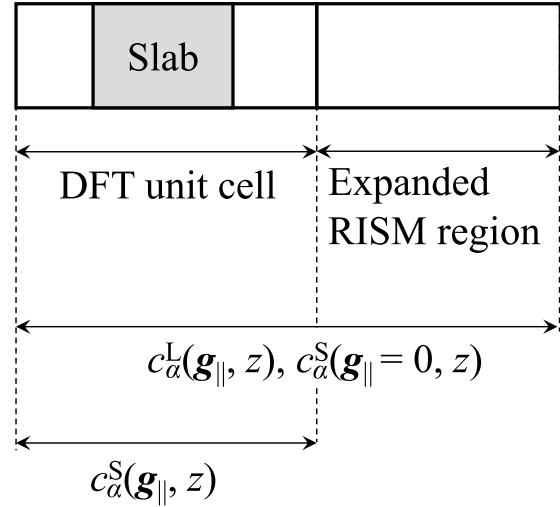


FIG. 9. Schematic of computational cell for ESM-RISM with the VSS boundary condition. The gray shaded area denotes the slab region. An expanded RISM region attached to the right edge of the DFT unit cell is depicted by a right box.

$$v_{\text{DFT}}(\mathbf{g}) = v_{\text{H}}(\mathbf{g}) + v_{\text{ion}}(\mathbf{g}). \quad (\text{B3})$$

Here, q_α and τ indicate the charges of each atomic site belonging to the implicit system and Coulomb smearing parameter, respectively. Typically, $\tau = 1.0$ Å is used in RISM calculations [39,40]. v_{DFT} is the electrostatic potential of the explicit system, which corresponds to the sum of Hartree and local parts of the ionic potentials (v_{H} and v_{ion}). $u_\alpha^L(\mathbf{g})$ can be determined before the 3D-RISM iteration. Thus, the iterative calculation in 3D-RISM optimizes $c_\alpha^S(\mathbf{r})$.

In ESM-RISM, we also separate $c_\alpha(\mathbf{g}_{\parallel}, z)$ into short- and long-range components for stable calculation using the following two processes. First, we separated the short- and long-range components using Eqs. (B2) and (B3). Then, the asymptotic behavior of the Laue-represented long-range component is determined using the ESM technique.

APPENDIX C: EXTENSION SCHEME FOR SHORT-RANGE DIRECT CORRELATION FUNCTION

In previous ESM-RISM calculations, all authors used an expanded RISM region attached to the DFT unit cell, as shown in Fig. 9, where we present the VSS boundary condition for simplicity. Here, we discuss a speed-up method to solve the LRISM equation with an expanded RISM region, as shown in Eq. (10). To reduce the computational cost, we focused on the calculation regions of the convolution integrals for $c_\alpha^S(\mathbf{g}_{\parallel}, z)$ and $c_\alpha^L(\mathbf{g}_{\parallel}, z)$.

To understand how to solve the LRISM equation, we first substitute Eq. (B1) into Eq. (10); we obtain

$$h_\gamma(\mathbf{g}_{\parallel}, z) = \sum_{\alpha} \left\{ \int dz' c_\alpha^S(\mathbf{g}_{\parallel}, z') \chi_{\alpha\gamma}(\mathbf{g}_{\parallel}, |z - z'|) + \int dz' c_\alpha^L(\mathbf{g}_{\parallel}, z') \chi_{\alpha\gamma}(\mathbf{g}_{\parallel}, |z - z'|) \right\}. \quad (\text{C1})$$

Because we can determine the long-range part by the one-shot calculation before the iteration of LRISM, it is a relatively small computational cost to evaluate the second term on the right-hand side of Eq. (C1). For a precise evaluation of the convolution integral for the long-range part, we define $c_\alpha^L(\mathbf{g}_\parallel, z)$ in the whole calculation cell, i.e., the DFT unit cell plus the expanded RISM region. Therefore, to accelerate the LRISM calculation, we must reduce the computational cost for the convolution integral of the short-range part.

Now, we consider the asymptotic behavior of $c_\alpha^S(\mathbf{g}_\parallel, z)$ for $z \rightarrow \infty$, which corresponds to $c_\alpha^S(\mathbf{g}_\parallel, z \rightarrow \infty) \rightarrow 0$. As after the convergence of the LRISM calculation, $c_\alpha^S(\mathbf{g}_\parallel, z)$ may converge into the DFT unit cell, we can define $c_\alpha^S(\mathbf{g}_\parallel, z)$ in the DFT unit cell as the first approximation. However, we found that the tail of $c_\alpha^S(\mathbf{g}_\parallel, z)$ is sometimes beyond the DFT cell edge, depending on the solution parameters, which provides numerical instability of the LRISM iteration. Therefore, we extended the calculation region of $c_\alpha^S(\mathbf{g}_\parallel = 0, z)$ to the expanded RISM region. In this region, we set the $\mathbf{g}_\parallel \neq 0$ components of c_α^S to zero, which indicates no lateral fluctuation of the $c_\alpha^S(\mathbf{r})$. Using the extension scheme discussed above for c_α^S , we successfully reduced the computational cost for calculating the LRISM equation.

APPENDIX D: CONSTRAINT TECHNIQUE FOR STOICHIOMETRY OF RISM PARTICLES

In ESM-RISM, we determine the number of RISM components under the grand-canonical condition through the numerical integration of the total correlation function. During the iteration for solving the LRISM equation, the stoichiometry of RISM components sometimes deviates from the input value beyond the number of counter ions and the numerical accuracy, which affects the stable convergence and numerical result. Therefore, we performed iterative LRISM calculations by imposing a constraint on the stoichiometry of the RISM components.

Here, we explain the stoichiometric constraint method for the RISM components, assuming the VSS boundary condition as a representative. We corrected the total correlation function to hold the stoichiometry as follows:

$$h_\alpha(\mathbf{g}_\parallel, z) = h'_\alpha(\mathbf{g}_\parallel, z) + \eta_\alpha w_\alpha(z), \quad (\text{D1})$$

where $h'_\alpha(\mathbf{g}_\parallel, z)$ and η_α indicate the total correlation function before correction and the stoichiometric coefficient, respectively. $w_\alpha(z)$ is a weight function and we assume the following form for $w_\alpha(z)$:

$$w_\alpha(z) = \text{erfc}\{(z - z_t)/\sigma_w\}/2.$$

Here, z_t is the tail position of $h_\alpha(\mathbf{g}_\parallel = 0, z)$, where $h_\alpha(\mathbf{g}_\parallel = 0, z_t) = 0$, and σ_w is a smearing factor, which is adjusted to be 2.0 bohrs. The number of atoms at the α site N'_α is obtained using the total correlation function before the correction by

$$N'_\alpha = S\rho_\alpha \int dz \{h'_\alpha(\mathbf{g}_\parallel = 0, z) + 1\}, \quad (\text{D2})$$

where S is the area in the lateral direction and the second term in the integral denotes the conversion factor from $h_\alpha(\mathbf{g}_\parallel = 0, z)$ to $g_\alpha(\mathbf{g}_\parallel = 0, z)$. The ‘‘correct’’ number of atoms at the

α site N_α should satisfy the following relation:

$$\begin{aligned} N_\alpha &= S\rho_\alpha \int dz \{h_\alpha(\mathbf{g}_\parallel = 0, z) + 1\} \\ &= \tilde{N}_M = \sum_\alpha^{N_M} N_\alpha/N_M, \end{aligned} \quad (\text{D3})$$

where N_M and \tilde{N}_M denote the total number of atoms belonging to molecule M and the average number of atoms in M , respectively. Therefore, η_α must be determined to satisfy Eq. (D3). By substituting Eq. (D1) into Eq. (D2), we obtain

$$N'_\alpha = \tilde{N}_M - S\rho_\alpha \int dz \eta_\alpha w_\alpha(z).$$

Hence, we obtain η_α as follows:

$$\eta_\alpha = \frac{\tilde{N}_M - N'_\alpha}{S\rho_\alpha \int dz w_\alpha(z)}. \quad (\text{D4})$$

As discussed previously, as a result of Eqs. (D1) and (D4), we correct the stoichiometry of the total correlation function obtained using Eq. (10), which contributed to the rapid convergence of the LRISM iteration.

APPENDIX E: LENNARD-JONES POTENTIAL WALL

In ESM-RISM, the distribution function of the solution permeates the interstitial regions of the electrode, depending on the morphology of the electrode and the force field parameters, which sometimes provide unphysical results. Therefore, we employed the following LJ-type repulsive potential wall $u_\alpha^{\text{wall}}(\mathbf{r})$:

$$\begin{aligned} u_\alpha^{\text{wall}}(\mathbf{r}) &= 4\rho_{\text{wall}} \sqrt{\epsilon_{\text{wall}} \epsilon_\alpha} \int_{-\infty}^{\infty} dx' \int_{-\infty}^{\infty} dy' \\ &\times \int_{-\infty}^{z_r} dz' \left\{ \frac{(\sigma_{\text{wall}} + \sigma_\alpha)/2}{|\mathbf{r} - \mathbf{r}'|} \right\}^{12}, \end{aligned} \quad (\text{E1})$$

where ρ_{wall} and z_r are the densities of the LJ wall and its right edge position, respectively. ϵ and σ are the LJ parameters and the subscript ‘‘wall’’ denotes the wall site. Note that ρ_{wall} only indicates the tuning parameter of the wall potential, which is adjustable determined to 0.01 bohr⁻³. Additionally, ϵ_{wall} and σ_{wall} were determined to be 0.1 kcal/mol and 4.0 Å, respectively. The analytical solution to Eq. (E1) is expressed as

$$u_\alpha^{\text{wall}}(\mathbf{r}) = \begin{cases} \infty, & z \leq z_r, \\ 8\pi\rho_{\text{wall}} \sqrt{\epsilon_{\text{wall}} \epsilon_\alpha} \frac{\{(\sigma_{\text{wall}} + \sigma_\alpha)/2\}^{12}}{90(z - z_r)}, & z > z_r. \end{cases} \quad (\text{E2})$$

Practically, we apply the wall potential to the ESM-RISM calculation using the pair-potential term in the closure function.

APPENDIX F: PROOF OF JANAK THEOREM WITHIN THE ESM-RISM FRAMEWORK

The Janak theorem for ordinal DFT can be written as [85]

$$\frac{\partial E_{\text{DFT}}[n]}{\partial f_{ik}} = \epsilon_{ik}, \quad (\text{F1})$$

where f_{ik} and ϵ_{ik} represent the occupation number and the KS eigenvalue, respectively. The index i denotes the com-

bined index of the bands and spins. In this Appendix, we first prove the Janak theorem within the 3D-RISM and ESM-RISM frameworks, and then discuss the potential origin shift used in the excess surface charge calculation in ESM-RISM.

First, we explicitly express the total Helmholtz free energy functional [Eq. (7)] as

$$\begin{aligned} A[n, \{\rho_\alpha\}] = & T_s[n] + \int d\mathbf{r} v_{\text{ion}}(\mathbf{r})n(\mathbf{r}) \\ & + \frac{1}{2} \int d\mathbf{r} d\mathbf{r}' \frac{n(\mathbf{r})n(\mathbf{r}')}{|\mathbf{r} - \mathbf{r}'|} + E_{\text{xc}}[n] \\ & + \Delta\mu_{\text{solv}}[n, \{\rho_\alpha\}]. \end{aligned} \quad (\text{F2})$$

Here, $T_s[n]$, $n(\mathbf{r})$, and $E_{\text{xc}}[n]$ represent the noninteractive kinetic energy functional, electron density, and exchange-correlation energy functional, respectively. The KS effective potential $v_{\text{eff}}(\mathbf{r})$ in 3D-RISM and ESM-RISM is expressed as

$$v_{\text{eff}}(\mathbf{r}) = v_{\text{H}}(\mathbf{r}) + v_{\text{ion}}(\mathbf{r}) + v_{\text{xc}}(\mathbf{r}) + v_{\text{solv}}(\mathbf{r}). \quad (\text{F3})$$

Here, $v_{\text{solv}}(\mathbf{r})$ and $v_{\text{xc}}(\mathbf{r})$ denote the exchange correlation and solution potentials, respectively. $v_{\text{solv}}(\mathbf{r})$ can be written as

$$v_{\text{solv}}(\mathbf{r}) = \frac{\delta \Delta\mu_{\text{solv}}[n, \{\rho_\alpha\}]}{\delta n(\mathbf{r})} = \int d\mathbf{r}' \frac{\rho_{\text{solv}}(\mathbf{r}')}{|\mathbf{r} - \mathbf{r}'|}, \quad (\text{F4})$$

$$\rho_{\text{solv}}(\mathbf{r}) = \sum_{\alpha} q_{\alpha} \rho_{\alpha} g_{\alpha}(\mathbf{r}), \quad (\text{F5})$$

where $\rho_{\text{solv}}(\mathbf{r})$ is the solution charge density and q_{α} denotes the charge of the RISM components. $g_{\alpha}(\mathbf{r})$ is the pair correlation function of the ESM-RISM (3D-RISM). By using f_{ik} , we define both $n(\mathbf{r})$ and $T_s[n]$ as follows:

$$n(\mathbf{r}) = \sum_{ik} f_{ik} |\psi_{ik}(\mathbf{r})|^2, \quad (\text{F6})$$

$$T_s[n] = \sum_{ik} f_{ik} \int d\mathbf{r} \psi_{ik}^*(\mathbf{r}) \left[-\frac{\nabla^2}{2} \right] \psi_{ik}(\mathbf{r}), \quad (\text{F7})$$

where $\psi_{ik}(\mathbf{r})$ represents the KS wave function. By substituting the KS equation into Eq. (F7), we obtain

$$T_s[n] = \sum_{ik} f_{ik} \epsilon_{ik} - \int d\mathbf{r} v_{\text{eff}}(\mathbf{r})n(\mathbf{r}). \quad (\text{F8})$$

Here, ϵ_{ik} and $v_{\text{eff}}(\mathbf{r})$ indicate the KS eigenvalue and the effective potential, respectively. The occupation derivatives of $n(\mathbf{r})$ and $T_s[n]$ are

$$\frac{\partial n(\mathbf{r})}{\partial f_{ik}} = |\psi_{ik}(\mathbf{r})|^2, \quad (\text{F9})$$

$$\frac{\partial T_s[n]}{\partial f_{ik}} = \epsilon_{ik} - \int d\mathbf{r} v_{\text{eff}}(\mathbf{r}) |\psi_{ik}(\mathbf{r})|^2. \quad (\text{F10})$$

The occupation derivative of the Helmholtz free energy functional shown in Eq. (F2) can be written as

$$\begin{aligned} \frac{\partial A[n, \{\rho_\alpha\}]}{\partial f_{ik}} = & \frac{\partial T_s[n]}{\partial f_{ik}} + \frac{\partial}{\partial f_{ik}} \int d\mathbf{r} v_{\text{ion}}(\mathbf{r})n(\mathbf{r}) \\ & + \frac{1}{2} \frac{\partial}{\partial f_{ik}} \int d\mathbf{r} d\mathbf{r}' \frac{n(\mathbf{r})n(\mathbf{r}')}{|\mathbf{r} - \mathbf{r}'|} \\ & + \frac{\partial E_{\text{xc}}[n]}{\partial f_{ik}} + \frac{\partial \Delta\mu_{\text{solv}}[n, \{\rho_\alpha\}]}{\partial f_{ik}}. \end{aligned} \quad (\text{F11})$$

Then, a part of Eq. (F11) can be written in the functional derivative form as follows:

$$\begin{aligned} \frac{\partial A[n, \{\rho_\alpha\}]}{\partial f_{ik}} = & \frac{\partial T_s[n]}{\partial f_{ik}} \\ & + \int |\psi_{ik}(\mathbf{r}')|^2 \frac{\delta}{\delta n(\mathbf{r}')} \left\{ \int d\mathbf{r} v_{\text{ion}}(\mathbf{r})n(\mathbf{r}) \right. \\ & + \frac{1}{2} \int d\mathbf{r} d\mathbf{r}' \frac{n(\mathbf{r})n(\mathbf{r}')}{|\mathbf{r} - \mathbf{r}'|} + E_{\text{xc}}[n] \\ & \left. + \Delta\mu_{\text{solv}}[n, \{\rho_\alpha\}] \right\} d\mathbf{r}'. \end{aligned} \quad (\text{F12})$$

Therefore, we obtain

$$\begin{aligned} \frac{\partial A[n, \{\rho_\alpha\}]}{\partial f_{ik}} = & \frac{\partial T_s[n]}{\partial f_{ik}} + \int |\psi_{ik}(\mathbf{r})|^2 \{v_{\text{ion}}(\mathbf{r}) \\ & + v_{\text{H}}(\mathbf{r}) + v_{\text{xc}}(\mathbf{r}) + v_{\text{solv}}(\mathbf{r})\} d\mathbf{r} \\ = & \frac{\partial T_s[n]}{\partial f_{ik}} + \int |\psi_{ik}(\mathbf{r})|^2 v_{\text{eff}}(\mathbf{r}) d\mathbf{r}. \end{aligned} \quad (\text{F13})$$

Here, $\frac{\delta E_{\text{xc}}[n]}{\delta n(\mathbf{r})} = v_{\text{xc}}(\mathbf{r})$, and we used Eq. (F3) for final equality. Finally, by substituting Eq. (F10) into Eq. (F13), we obtain the following Janak theorem within the 3D-RISM and ESM-RISM frameworks:

$$\frac{\partial A[n, \{\rho_\alpha\}]}{\partial f_{ik}} = \epsilon_{ik}. \quad (\text{F14})$$

This result indicates that the relation in Eq. (21) is guaranteed by the Janak theorem for the 3D-RISM and ESM-RISM. For the proof of the Janak theorem, the Helmholtz free energy functional needs to be consistent with the KS effective potential obtained by the functional derivative, which is found in Eqs. (F12) and (F13).

In the ESM-RISM calculation for a half-cell system, we always consider the inner potential as the origin of the energy level. In convenience, here, we consider the calculation cell with the vacuum/slab/solution boundary condition. However, in the mixed-boundary condition, the origin of the electrostatic potential is chosen as its midpoint between the left and right sides of the $\mathbf{g}_{\parallel} = 0$ components [33]. Therefore, to obtain the reference potential, we shift the average of the total electrostatic potential inside the RISM solution v_{DFT} to zero, which requires introducing the correction term for the Helmholtz free energy functional. For simplicity, we rewrite the Helmholtz free energy functional as follows:

$$A = T_s + E_{\text{es}} + E_{\text{xc}} + \Delta\mu_{\text{solv}}, \quad (\text{F15})$$

where E_{es} denotes the electrostatic energy, which is the sum of the Hartree and ionic energies. The correction term arises from the electrostatic potential shift in v_{DFT} .

Here, we discuss the correction term for the Helmholtz free energy functional due to the potential shift, which needs to retain the relationship shown in Eq. (21) for ESM-RISM using the inner potential technique. When v_{DFT} at the right edge of the RISM region is v_0 , we shift v_{DFT} by

$$v'_{\text{DFT}}(\mathbf{g}_{\parallel} = 0, z) = v_{\text{DFT}}(\mathbf{g}_{\parallel} = 0, z) - v_0. \quad (\text{F16})$$

Therefore, the electrostatic energy E_{es} is modified as

$$E'_{\text{es}} = E_{\text{es}} - v_0 \Delta N. \quad (\text{F17})$$

Here, we only considered the number of excess electrons ΔN . Furthermore, the potential shift alters $\Delta\mu_{\text{solv}}$ because the asymptotic behavior of the direct correlation function depends on v_{DFT} . Here, we discuss the energy shift of $\Delta\mu_{\text{solv}}$ using the Gaussian fluctuation model [76]. In the Gaussian fluctuation model, $\Delta\mu_{\text{solv}}$ was calculated as follows:

$$\Delta\mu_{\text{solv}} = \frac{1}{\beta} \sum_{\alpha} \rho_{\alpha} \int d\mathbf{r} \left[-c_{\alpha}(\mathbf{r}) - \frac{1}{2} h_{\alpha}(\mathbf{r}) c_{\alpha}(\mathbf{r}) \right]. \quad (\text{F18})$$

Because the long-range part of $c_{\alpha}(\mathbf{r})$ depends on $v_{\text{DFT}}(\mathbf{r})$, the potential shift procedure should be applied to $\Delta\mu_{\text{solv}}$. Therefore, after the potential shift procedure, we obtain

$$\begin{aligned} \Delta\mu'_{\text{solv}} &= \frac{1}{\beta} \sum_{\alpha} \rho_{\alpha} \int d\mathbf{r} \left[-\{c_{\alpha}(\mathbf{r}) - \beta q_{\alpha} v_0\} \right. \\ &\quad \left. - \frac{1}{2} h_{\alpha}(\mathbf{r}) \{c_{\alpha}(\mathbf{r}) - \beta q_{\alpha} v_0\} \right] \\ &= \Delta\mu_{\text{solv}} \\ &\quad + \frac{1}{2} \sum_{\alpha} \rho_{\alpha} q_{\alpha} v_0 \int d\mathbf{r} \{1 + g_{\alpha}(\mathbf{r})\}, \quad (\text{F19}) \end{aligned}$$

where $g_{\alpha}(\mathbf{r}) = h_{\alpha}(\mathbf{r}) + 1$ in the final equality. The second term becomes zero because of the charge-neutral condition of the bulk solution, and using Eq. (F5), the third term can be

rewritten as

$$\begin{aligned} \frac{1}{2} \sum_{\alpha} \rho_{\alpha} q_{\alpha} v_0 \int d\mathbf{r} g_{\alpha}(\mathbf{r}) &= \frac{v_0}{2} \int d\mathbf{r} \rho_{\text{solv}}(\mathbf{r}) \\ &= \frac{v_0 \Delta Q_{\text{RISM}}}{2}. \quad (\text{F20}) \end{aligned}$$

Here, ΔQ_{RISM} indicates the number of counter ions to screen the excess surface charge owing to the charge-neutral condition for the entire (explicit + implicit) system. Because $\Delta Q_{\text{RISM}} = \Delta N$, we obtain

$$\Delta\mu'_{\text{solv}} = \Delta\mu_{\text{solv}} + \frac{v_0 \Delta N}{2}. \quad (\text{F21})$$

Therefore, the total energy correction term owing to the potential shift can be obtained as the third term on the right-hand side of the following equation:

$$E'_{\text{es}} + \Delta\mu'_{\text{solv}} = E_{\text{es}} + \Delta\mu_{\text{solv}} - \frac{v_0 \Delta N}{2}. \quad (\text{F22})$$

After the correction, we finally obtain the Helmholtz free energy functional as

$$A = T_s + E_{\text{es}} + E_{\text{xc}} + \Delta\mu_{\text{solv}} - \frac{v_0 \Delta N}{2}. \quad (\text{F23})$$

Here, we note that the potential shift term is only required for the charged system, and by this correction, the Helmholtz free energy functional becomes consistent with v_{eff} with and without the excess charge. Because of this correction, the Janak theorem holds in the ESM-RISM calculation using the inner potential technique. Haruyama *et al.* used this correction term to numerically verify Eq. (21) [59].

-
- [1] J. Klankermayer, S. Wesselbaum, K. Beydoun, and W. Leitner, *Angew. Chem. Int. Ed.* **55**, 7296 (2016).
- [2] R. Asri, W. Harun, M. Samykano, N. Lah, S. Ghani, F. Tarlochan, and M. Raza, *Mater. Sci. Eng. C* **77**, 1261 (2017).
- [3] A. Kulkarni, S. Siahrostami, A. Patel, and J. K. Nørskov, *Chem. Rev.* **118**, 2302 (2018).
- [4] A. M. Tripathi, W.-N. Su, and B. J. Hwang, *Chem. Soc. Rev.* **47**, 736 (2018).
- [5] M. Otani, I. Hamada, O. Sugino, Y. Morikawa, Y. Okamoto, and T. Ikeshoji, *J. Phys. Soc. Jpn.* **77**, 024802 (2008).
- [6] T. Ikeshoji, M. Otani, I. Hamada, and Y. Okamoto, *Phys. Chem. Chem. Phys.* **13**, 20223 (2011).
- [7] Y. Ando, Y. Gohda, and S. Tsuneyuki, *Chem. Phys. Lett.* **556**, 9 (2013).
- [8] A. d'Entremont and L. Pilon, *J. Power Sources* **246**, 887 (2014).
- [9] T. Ikeshoji and M. Otani, *Phys. Chem. Chem. Phys.* **19**, 4447 (2017).
- [10] T. Tamura, M. Kohyama, and S. Ogata, *Phys. Rev. B* **96**, 035107 (2017).
- [11] T. Ohto, M. Dodia, S. Imoto, and Y. Nagata, *J. Chem. Theory Comput.* **15**, 595 (2018).
- [12] T. Kaneko and K. Sodeyama, *Chem. Phys. Lett.* **762**, 138199 (2021).
- [13] A. Klamt and G. Schüürmann, *J. Chem. Soc., Perkin Trans. 2* **1993**, 799 (1993).
- [14] V. Barone and M. Cossi, *J. Phys. Chem. A* **102**, 1995 (1998).
- [15] A. V. Marenich, C. J. Cramer, and D. G. Truhlar, *J. Phys. Chem. B* **113**, 6378 (2009).
- [16] A. Klamt, F. Eckert, and W. Arlt, *Annu. Rev. Chem. Biomol. Eng.* **1**, 101 (2010).
- [17] O. Andreussi, I. Dabo, and N. Marzari, *J. Chem. Phys.* **136**, 064102 (2012).
- [18] R. Sundararaman and W. A. Goddard III, *J. Chem. Phys.* **142**, 064107 (2015).
- [19] K. Schwarz and R. Sundararaman, *Surf. Sci. Rep.* **75**, 100492 (2020).
- [20] A. M. Maldonado, S. Hagiwara, T. H. Choi, F. Eckert, K. Schwarz, R. Sundararaman, M. Otani, and J. A. Keith, *J. Phys. Chem. A* **125**, 154 (2021).
- [21] J. A. Gauthier, S. Ringe, C. F. Dickens, A. J. Garza, A. T. Bell, M. Head-Gordon, J. K. Nørskov, and K. Chan, *ACS Catal.* **9**, 920 (2019).
- [22] N. Shao, X.-G. Sun, S. Dai, and D.-e. Jiang, *J. Phys. Chem. B* **115**, 12120 (2011).
- [23] O. Borodin, *Curr. Opin. Electrochem.* **13**, 86 (2019).
- [24] R. Sundararaman, W. A. Goddard, III, and T. A. Arias, *J. Chem. Phys.* **146**, 114104 (2017).
- [25] F. Li, H. Wen, and Q. Tang, *J. Mater. Chem. A* **10**, 13266 (2022).
- [26] T. Gaudin and J.-M. Aubry, *J. Energy Storage* **49**, 104152 (2022).

- [27] N. G. Hörmann, Z. Guo, F. Ambrosio, O. Andreussi, A. Pasquarello, and N. Marzari, *npj Comput. Mater.* **5**, 100 (2019).
- [28] F. Hirata and P. J. Rossky, *Chem. Phys. Lett.* **83**, 329 (1981).
- [29] F. Hirata, B. M. Pettitt, and P. J. Rossky, *J. Chem. Phys.* **77**, 509 (1982).
- [30] F. Hirata, P. J. Rossky, and B. M. Pettitt, *J. Chem. Phys.* **78**, 4133 (1983).
- [31] P. Hohenberg and W. Kohn, *Phys. Rev.* **136**, B864 (1964).
- [32] W. Kohn and L. J. Sham, *Phys. Rev.* **140**, A1133 (1965).
- [33] M. Otani and O. Sugino, *Phys. Rev. B* **73**, 115407 (2006).
- [34] I. Hamada, M. Otani, O. Sugino, and Y. Morikawa, *Phys. Rev. B* **80**, 165411 (2009).
- [35] N. Bonnet, T. Morishita, O. Sugino, and M. Otani, *Phys. Rev. Lett.* **109**, 266101 (2012).
- [36] I. Hamada, O. Sugino, N. Bonnet, and M. Otani, *Phys. Rev. B* **88**, 155427 (2013).
- [37] S. Hagiwara, C. Hu, S. Nishihara, and M. Otani, *Phys. Rev. Mater.* **5**, 065001 (2021).
- [38] S. Nishihara and M. Otani, *Phys. Rev. B* **96**, 115429 (2017).
- [39] A. Kovalenko and F. Hirata, *J. Chem. Phys.* **110**, 10095 (1999).
- [40] N. Yoshida, S. Phongphanphanee, Y. Maruyama, T. Imai, and F. Hirata, *J. Am. Chem. Soc.* **128**, 12042 (2006).
- [41] J. Haruyama, T. Ikeshoji, and M. Otani, *J. Phys. Chem. C* **122**, 9804 (2018).
- [42] T. Shimada, N. Takenaka, Y. Ando, M. Otani, M. Okubo, and A. Yamada, *Chem. Mater.* **34**, 2069 (2022).
- [43] J. S. Perkyns and B. M. Pettitt, *Chem. Phys. Lett.* **190**, 626 (1992).
- [44] J. Perkyns and B. M. Pettitt, *J. Chem. Phys.* **97**, 7656 (1992).
- [45] G. Schmeer and A. Maurer, *Phys. Chem. Chem. Phys.* **12**, 2407 (2010).
- [46] I. S. Joung, T. Luchko, and D. A. Case, *J. Chem. Phys.* **138**, 044103 (2013).
- [47] D.-M. Duh and A. Haymet, *J. Chem. Phys.* **103**, 2625 (1995).
- [48] D.-M. Duh and D. Henderson, *J. Chem. Phys.* **104**, 6742 (1996).
- [49] A. Kovalenko and F. Hirata, *J. Chem. Phys.* **112**, 10391 (2000).
- [50] Y. Ikuta and F. Hirata, *J. Mol. Liq.* **294**, 111567 (2019).
- [51] T. Morita, *Prog. Theor. Phys.* **20**, 920 (1958).
- [52] T. Morita, *Prog. Theor. Phys.* **21**, 361 (1959).
- [53] K. Kim, Y. Ando, A. Sugahara, S. Ko, Y. Yamada, M. Otani, M. Okubo, and A. Yamada, *Chem. Mater.* **31**, 5190 (2019).
- [54] A. Sugahara, Y. Ando, S. Kajiyama, K. Yazawa, K. Gotoh, M. Otani, M. Okubo, and A. Yamada, *Nat. Commun.* **10**, 850 (2019).
- [55] Y. Ando, M. Okubo, A. Yamada, and M. Otani, *Adv. Funct. Mater.* **30**, 2000820 (2020).
- [56] S. Hagiwara, Y. Ando, Y. Goto, S. Shinoki, and M. Otani, *Phys. Rev. Mater.* **6**, 025001 (2022).
- [57] K. Yabana, T. Nakatsukasa, J.-I. Iwata, and G. Bertsch, *Phys. Status Solidi B* **243**, 1121 (2006).
- [58] S. A. Sato, *J. Phys.: Condens. Matter* **34**, 095903 (2021).
- [59] J. Haruyama, T. Ikeshoji, and M. Otani, *Phys. Rev. Mater.* **2**, 095801 (2018).
- [60] NIST-JANAF, <https://janaf.nist.gov>.
- [61] K. Kano, S. Hagiwara, T. Igarashi, and M. Otani, *Electrochim. Acta* **377**, 138121 (2021).
- [62] S. E. Weitzner, S. A. Akhade, J. B. Varley, B. C. Wood, M. Otani, S. E. Baker, and E. B. Duoss, *J. Phys. Chem. Lett.* **11**, 4113 (2020).
- [63] T. Saito, T. Yokoi, A. Nakamura, and K. Matsunaga, *RSC Adv.* **11**, 34004 (2021).
- [64] K. Momma and F. Izumi, *J. Appl. Crystallogr.* **41**, 653 (2008).
- [65] K. Momma and F. Izumi, *J. Appl. Crystallogr.* **44**, 1272 (2011).
- [66] P. Giannozzi, S. Baroni, N. Bonini, M. Calandra, R. Car, C. Cavazzoni, D. Ceresoli, G. L. Chiarotti, M. Cococcioni, I. Dabo *et al.*, *J. Phys.: Condens. Matter* **21**, 395502 (2009).
- [67] P. Giannozzi, O. Andreussi, T. Brumme, O. Bunau, M. B. Nardelli, M. Calandra, R. Car, C. Cavazzoni, D. Ceresoli, M. Cococcioni *et al.*, *J. Phys.: Condens. Matter* **29**, 465901 (2017).
- [68] D. Vanderbilt, *Phys. Rev. B* **41**, 7892 (1990).
- [69] K. Laasonen, R. Car, C. Lee, and D. Vanderbilt, *Phys. Rev. B* **43**, 6796 (1991).
- [70] K. Laasonen, A. Pasquarello, R. Car, C. Lee, and D. Vanderbilt, *Phys. Rev. B* **47**, 10142 (1993).
- [71] J. P. Perdew, K. Burke, and M. Ernzerhof, *Phys. Rev. Lett.* **77**, 3865 (1996).
- [72] S. G. Louie, S. Froyen, and M. L. Cohen, *Phys. Rev. B* **26**, 1738 (1982).
- [73] AtomWork, <https://crystdb.nims.go.jp>.
- [74] M. J. Frisch, G. W. Trucks, H. B. Schlegel, G. E. Scuseria, M. A. Robb, J. R. Cheeseman, G. Scalmani, V. Barone, G. A. Petersson, H. Nakatsuji *et al.*, Gaussian 16, Revision C.01, Gaussian, Inc., Wallingford, CT.
- [75] A. Kovalenko, S. Ten-no, and F. Hirata, *J. Comput. Chem.* **20**, 928 (1999).
- [76] R. M. Levy, M. Belhadj, and D. B. Kitchen, *J. Chem. Phys.* **95**, 3627 (1991).
- [77] H. A. Lorentz, *Ann. Phys.* **248**, 127 (1881).
- [78] D. Berthelot, *C. R. Acad. Sci. Paris* **126**, 1703 (1898).
- [79] T. Luchko, S. Gusarov, D. R. Roe, C. Simmerling, D. A. Case, J. Tuszynski, and A. Kovalenko, *J. Chem. Theory Comput.* **6**, 607 (2010).
- [80] I. S. Joung and T. E. Cheatham, III, *J. Phys. Chem. B* **112**, 9020 (2008).
- [81] D. J. Bonthuis, S. I. Mamatkulov, and R. R. Netz, *J. Chem. Phys.* **144**, 104503 (2016).
- [82] *CRC handbook of Chemistry and Physics*, 102nd ed., edited by J. R. Rumble (CRC Press, 2021).
- [83] A. Ben-Naim and Y. Marcus, *J. Chem. Phys.* **81**, 2016 (1984).
- [84] R. Tesch, P. M. Kowalski, and M. H. Eikerling, *J. Phys.: Condens. Matter* **33**, 444004 (2021).
- [85] J. F. Janak, *Phys. Rev. B* **18**, 7165 (1978).
- [86] A. Cuesta, *Surf. Sci.* **572**, 11 (2004).
- [87] T. Pajkossy and D. Kolb, *Electrochim. Acta* **46**, 3063 (2001).
- [88] N. Garcia-Araez, V. Climent, E. Herrero, J. M. Felio, and J. Lipkowski, *Electrochim. Acta* **51**, 3787 (2006).
- [89] S. Trasatti, *Pure Appl. Chem.* **58**, 955 (1986).
- [90] S. Trasatti, *Electrochim. Acta* **36**, 1659 (1991).
- [91] *IUPAC Compendium of Chemical Terminology*, 2nd ed. (the "Gold Book"), compiled by A. D. McNaught and A. Wilkinson (Blackwell Scientific, Oxford, 1997).
- [92] A. Frumkin, O. Petry, and B. Damaskin, *J. Electroanal. Chem. Interfacial Electrochem.* **27**, 81 (1970).
- [93] D. Kramer and J. Weissmüller, *Surf. Sci.* **601**, 3042 (2007).
- [94] N. Lang and W. Kohn, *Phys. Rev. B* **7**, 3541 (1973).
- [95] K. Ojha, N. Arulmozhi, D. Aranzales, and M. T. Koper, *Angew. Chem.* **132**, 721 (2020).
- [96] K. Ojha, K. Doblhoff-Dier, and M. T. Koper, *Proc. Natl. Acad. Sci. USA* **119**, e2116016119 (2022).